

Softening and residual loss modulus of jammed grains under oscillatory shear in absorbing state

Michio Otsuki*

Graduate School of Engineering Science, Osaka University, Toyonaka, Osaka 560-8531, Japan

Hisao Hayakawa

Yukawa Institute for Theoretical Physics, Kyoto University,
Kitashirakawaoiwake-cho, Sakyo-ku, Kyoto 606-8502, Japan

(Dated: December 23, 2024)

From a theoretical study of the mechanical response of jammed materials comprising frictionless and overdamped particles under oscillatory shear, we find that the material becomes soft, and the loss modulus remains finite even in an absorbing state where any irreversible plastic deformation does not exist. The trajectories of the particles in this region exhibit hysteresis loops. We succeed in clarifying the origin of the softening of the material and the residual loss modulus with the aid of Fourier analysis. We also clarify the roles of the yielding point in the softening to distinguish the plastic deformation from reversible deformation in the absorbing state.

Introduction— The mechanical response of jammed disordered materials, such as granular materials, foams, emulsions, and colloidal suspensions, garners much attention [1, 2]. For vanishingly small strain, the shear stress σ is proportional to the shear strain γ , which is characterized by the shear modulus satisfying a critical scaling law near the jamming point ϕ_J [3–5]. However, the region of the linear response is quite narrow near ϕ_J [6, 7]. Hence, revealing the nonlinear response is essential for understanding the dynamics of disordered materials.

In crystalline materials, the nonlinear response originates from yielding associated with irreversible plastic deformation. Yielding also takes place in disordered materials when the strain is sufficiently large [8–13]. The yielding transition attracts much attention among researchers as an example of the reversible-irreversible transition [14–17]. When plastic deformation causes rearrangements of contact networks, the mechanical response becomes nonlinear. It had been believed that plastic deformation is always necessary for the nonlinear response. Unlike this expectation, recent studies have revealed that plastic deformation is not always necessary for the nonlinear response [18–22]. Under steady shear, σ becomes hypoelastic before the yielding [18, 20], and the storage modulus in the steady state after applying a sufficient number of cyclic shears decreases as the strain amplitude increases without any irreversible plastic deformation [21]. The decrease of the storage modulus is called softening.

It is known that plastic deformation causes dissipation characterized by the loss modulus [21, 22]. It is natural that the loss modulus disappears in quasi-static strains without any plastic deformation. However, we need careful check of this naive picture, because the loss modulus might be related to the softening observed without any plastic deformation.

The mechanical response should be related to the motion of particles constituting the disordered materials. This suggests that the trajectories of particles provide information on the softening of the materials. Several studies have reported that the trajectories of dense particles form closed loops under oscillatory shear below the yielding point associated with reversible contact changes where there are some cyclic open and close contacts between particles [23–34]. The formation of closed loops means that the system is reduced to an absorbing state after some time has passed. A previous study numerically showed that the softening in the absorbing state becomes significant when there are closed loops associated with many contact changes. However, the quantitative relationship remains unclear [21].

In this study, we numerically investigate jammed materials comprising N frictionless and overdamped particles under oscillatory shear to clarify the origin of the softening. For this purpose, we focus on the roles of the trajectories to clarify the relationship between the softening in the absorbing state and the softening in the plastic regime. We find that the shear modulus exhibits softening, and the loss modulus remains finite even in the absorbing state below the yielding point. The trajectory of a test particle forms a nontrivial loop in this region. With the aid of Fourier analysis, we investigate the geometric structure of the trajectories and reveal the role of Fourier components for the storage and loss moduli. We also present the theoretical expressions for the storage and loss moduli, whose quantitative validities are numerically confirmed.

Setup— Let us consider a jammed two-dimensional system consisting of frictionless particles under oscillatory shear. The particles are driven by the overdamped equation with Stokes' drag under Lees–Edwards boundary conditions [35], where the equation of motion is given by

$$\zeta \left\{ \frac{d}{dt} \mathbf{r}_i - \dot{\gamma}(t) y_i \mathbf{e}_x \right\} = - \sum_{j \neq i} \frac{\partial}{\partial \mathbf{r}_i} U(r_{ij}) \quad (1)$$

*otsuki@me.es.osaka-u.ac.jp

with the position $\mathbf{r}_i = (x_i, y_i)$ of particle i . Here, ζ and $\dot{\gamma}(t)$ are the drag coefficient and strain rate, respectively. The interaction potential $U(r_{ij})$ is assumed to be

$$U(r_{ij}) = \frac{k}{2}(d_{ij} - r_{ij})^2 \Theta(d_{ij} - r_{ij}), \quad (2)$$

where $\Theta(x)$, k , d_{ij} , and $r_{ij} = |\mathbf{r}_{ij}| = |\mathbf{r}_i - \mathbf{r}_j|$ are the Heaviside step function satisfying $\Theta(x) = 1$ for $x \geq 0$ and $\Theta(x) = 0$ otherwise, the spring constant, the average diameter of particles i and j , and the distance between particles i and j , respectively. The system is bidisperse and consists of an equal number of particles with diameters d_0 and $d_0/1.4$. We have verified that particles with inertia and damping at contact, which corresponds to the model in Ref. [21], exhibit almost identical behavior in our system [36].

We prepare the initial state with a given packing fraction ϕ by slowly compressing the system from a state below the jamming point $\phi_J \simeq 0.841$ [5]. The oscillatory shear strain is applied for N_c cycles as

$$\gamma(\theta) = \gamma_0 \sin \theta \quad (3)$$

with the phase $\theta = \omega t$, where γ_0 and ω are the strain amplitude and angular frequency, respectively. The value of N_c will be discussed later. Note that the shear rate satisfies $\dot{\gamma}(t) = (d\theta/dt)(d/d\theta)\gamma(\theta)$. In the last cycle, we measure the storage and loss moduli G' and G'' , respectively, given by [37]

$$G' = \frac{1}{\pi} \int_0^{2\pi} d\theta \frac{\langle \sigma(\theta) \rangle \sin \theta}{\gamma_0}, \quad (4)$$

$$G'' = \frac{1}{\pi} \int_0^{2\pi} d\theta \frac{\langle \sigma(\theta) \rangle \cos \theta}{\gamma_0}, \quad (5)$$

with shear stress

$$\sigma = \frac{1}{L^2} \sum_i \sum_{j>i} \frac{x_{ij} y_{ij}}{r_{ij}} U'(r_{ij}), \quad (6)$$

where $x_{ij} = x_i - x_j$, $y_{ij} = y_i - y_j$, $\langle \cdot \rangle$ represents the ensemble average, and L is the linear system size. See Ref. [36] for the stress-strain curves in our system. We have verified that G' and G'' shown below are independent of N and N_c for $N \geq 1000$ and $N_c \geq 20$. Thus, we use $N = 1000$ and $N_c = 20$ in our numerical analysis. We adopt the Euler method using the time step $\Delta t = 0.05\tau_0$ with $\tau_0 = \zeta/k$.

Closed Trajectories— As the number of cycles increases, the system reaches a statistically steady state through a transient regime as shown in Ref. [36]. Figure 1 displays typical non-affine trajectories of a particle

$$\tilde{\mathbf{r}}_i(\theta) = \mathbf{r}_i(\theta) - \gamma(\theta) y_i(\theta) \mathbf{e}_x \quad (7)$$

in the last two cycles with $\phi = 0.87$ and $\omega = 10^{-4}\tau_0^{-1}$ in the steady state. The trajectories are closed, and the particle returns to its original position after every cycle.

This indicates that irreversible plastic deformation does not occur, at least in the last two cycles. The closed trajectories form nontrivial loops, which differ from ellipses or lines observed for small γ_0 as shown in Ref. [36]. In Fig. 1(b) ($\gamma_0 = 0.1$), the particle moves away from its original positions after a cycle, as a characteristic behavior of plastic deformation. Here, we define the absorbing state where the displacement of each particle after several cycles is smaller than $d_c = 10^{-4}d_0$ in the statistically steady state. We also define the plastic state where the displacement after several cycles exceeds d_c . It should be noted that some rare samples exhibit trajectories where particles return to their original positions after more than one cycle [27, 28, 30, 31, 33]. However, our theoretical results shown below are unchanged even if such samples exist, as shown in Ref. [36].

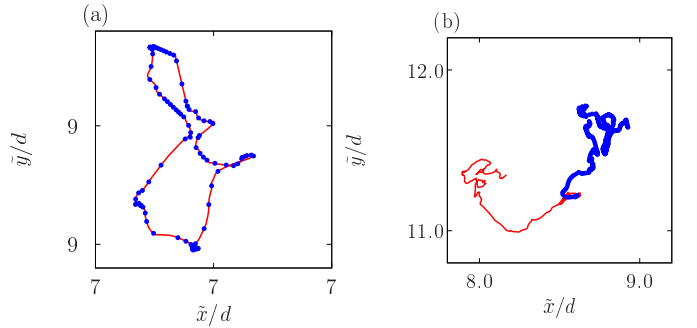


FIG. 1: Non-affine particle trajectories in the last two cycles for $\gamma_0 = 0.02$ (a) and 0.1 (b) with $\omega = 10^{-4}\tau_0^{-1}$ and $\phi = 0.87$, which corresponds to $\phi - \phi_J = 0.029$. The circles represent the trajectory in the last cycle. The line represents the trajectory in the second to the last cycle.

Shear Modulus— We plot the storage modulus G' against the strain amplitude γ_0 for $\omega = 10^{-4}\tau_0^{-1}$ with $\phi = 0.870, 0.860, 0.850$, and 0.845 in Fig. 2. The yielding points to distinguish the absorbing state from the plastic state for various ϕ are shown by open pentagons, which are estimated in Ref. [36]. The storage modulus G' decreases as γ_0 increases, but the yielding point is not identical to the point where G' starts to decrease. We call the decrease for $\gamma_0 < \gamma_c$, the yielding strain amplitude, the softening in the absorbing state (SAS). We also call the decrease for $\gamma_0 > \gamma_c$ the softening in the plastic state (SPS). It is remarkable that SAS is continuously connected to SPS, while a plateau in G' appears in SPS for systems near the jamming point ϕ_J . In the inset of Fig. 2, we demonstrate that G' and γ_0 can be scaled by $\sqrt{\phi - \phi_J}$ and $\phi - \phi_J$, respectively, as indicated in Refs. [3, 21]. We have confirmed that G' is independent of ω for $\omega \leq 10^{-3}\tau_0^{-1}$.

Figure 3(a) displays the loss modulus G'' in the absorbing state against γ_0 for $\omega = 10^{-4}\tau_0^{-1}$ with $\phi = 0.870, 0.860, 0.850$, and 0.845 , in which G'' does not strongly depend on ϕ and γ_0 . See Ref. [36] for G'' in the plastic state. In Fig. 3(b), we plot the loss modulus G'' in the absorbing state against ω for $\phi = 0.87$

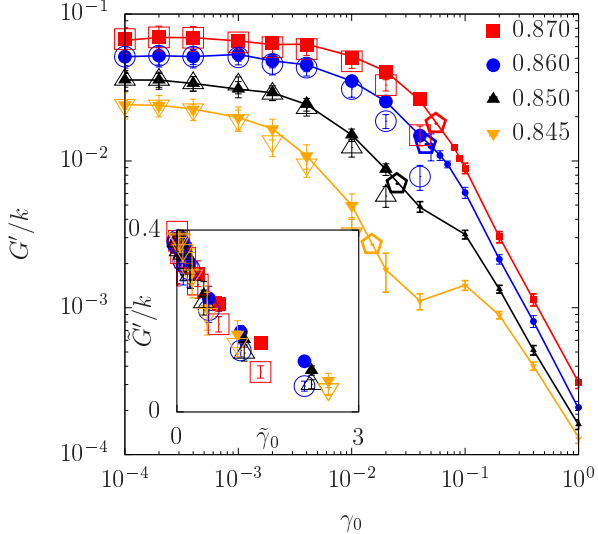


FIG. 2: Storage modulus G' obtained in our simulation (filled symbols) against γ_0 for $\omega = 10^{-4}\tau_0^{-1}$ with $\phi = 0.870, 0.860, 0.850$, and 0.845 , which corresponds to $\phi - \phi_J = 0.029, 0.019, 0.009$, and 0.004 , respectively. The legends represent the packing fraction ϕ . The data in the absorbing (plastic) state obtained in our simulation are shown in larger (smaller) filled symbols. The open pentagons represent the yielding strain amplitude γ_c , while other open symbols represent the theoretical expression using G'_T in Eq. (13). (Inset) Scaled storage modulus $\tilde{G}' = G'/\sqrt{\phi - \phi_J}$ obtained in our simulation (filled symbols) and its theoretical expression using G'_T (open symbols) in Eq. (13) against scaled strain amplitude $\tilde{\gamma}_0 = \gamma_0/(\phi - \phi_J)$ in the absorbing state.

with $\gamma = 0.01$. Remarkably, G'' in Fig. 3(b) seems to converge to a finite value in the limit $\omega \rightarrow 0$, which contrasts with the behavior of the Kelvin–Voigt model (i.e., $G'' \propto \omega$ [38]). This behavior indicates that dissipation remains even in the quasi-static limit in the absorbing state. Note that $G'' \propto \omega$ is recovered when we adopt a sufficiently small γ_0 [36].

Fourier Analysis— In the absorbing state, the non-affine trajectory $\tilde{r}_i(\theta)$ of particle i can be expressed in a Fourier series as

$$\tilde{r}_i(\theta) = \mathbf{R}_i + \sum_{n=1}^{\infty} \left(\mathbf{a}_i^{(n)} \sin n\theta + \mathbf{b}_i^{(n)} \cos n\theta \right) \quad (8)$$

with the center of the trajectory

$$\mathbf{R}_i = (X_i, Y_i) = \frac{1}{2\pi} \int_0^{2\pi} d\theta \tilde{r}_i(\theta), \quad (9)$$

and the Fourier coefficients

$$\mathbf{a}_i^{(n)} = \frac{1}{\pi} \int_0^{2\pi} d\theta \sin n\theta \tilde{r}_i(\theta), \quad (10)$$

$$\mathbf{b}_i^{(n)} = \frac{1}{\pi} \int_0^{2\pi} d\theta \cos n\theta \tilde{r}_i(\theta). \quad (11)$$

If $\mathbf{a}_i^{(n)} = \mathbf{b}_i^{(n)} = \mathbf{0}$ for all n , the particle motion is affine. When only $\mathbf{a}_i^{(1)}$ is finite, the non-affine trajectory is a

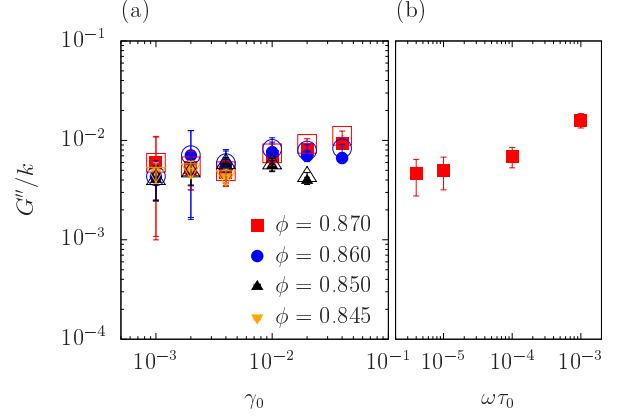


FIG. 3: (a) Loss modulus G'' in the absorbing state obtained in our simulation (filled symbols) and its theoretical expression G''_T (open symbols) in Eq. (14) against γ_0 for $\omega = 10^{-4}\tau_0^{-1}$ with $\phi = 0.870, 0.860, 0.850$, and 0.845 , which corresponds to $\phi - \phi_J = 0.029, 0.019, 0.009$, and 0.004 , respectively. (b) Loss modulus G'' against $\omega\tau_0$ for $\phi = 0.87$ with $\gamma_0 = 0.01$.

straight line, as shown in Fig. 4(a). In contrast, the trajectory exhibits an ellipse when $\mathbf{b}_i^{(1)}$ is also finite, as shown in Fig. 4(b). A nontrivial trajectory, as shown in Fig. 1(a), contains modes with $n \geq 2$. See Ref. [36] for the relationship between the trajectories and the Fourier coefficients.

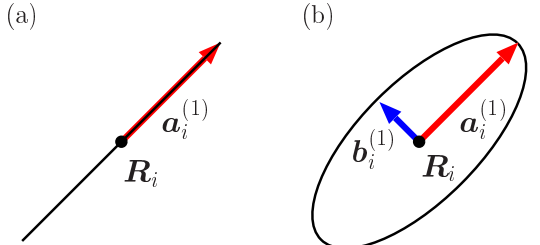


FIG. 4: Schematics of the non-affine trajectory when only $\mathbf{a}_i^{(1)}$ is finite (a) and only $\mathbf{a}_i^{(1)}$ and $\mathbf{b}_i^{(1)}$ are finite (b).

In Fig. 5(a), we plot the magnitudes of the Fourier components

$$a^{(n)} = \sum_i \left\langle \left| \mathbf{a}_i^{(n)} \right| \right\rangle / N, \quad b^{(n)} = \sum_i \left\langle \left| \mathbf{b}_i^{(n)} \right| \right\rangle / N \quad (12)$$

obtained from our numerical data using Eqs. (10) and (11) against n for $\phi = 0.87$ and $\gamma_0 = 0.01$ with $\omega\tau_0 = 10^{-4}$ and 10^{-5} . Here, $a^{(1)}$ takes the largest value, but the other components are also finite, which coincides with the existence of nontrivial loops presented in Fig. 1. The Fourier components do not strongly depend on ω , which indicates that the nontrivial loops do not disappear in the limit $\omega \rightarrow 0$. For different $\phi > \phi_J$ and $\gamma_0 \geq 10^{-3}$, we have confirmed that $a^{(1)}$ is always the largest, the other modes are finite, and the Fourier components are independent of ω . In Fig. 5(b), we plot $a^{(n)}/\gamma_0$ and $b^{(n)}/\gamma_0$ against γ_0

for $\phi = 0.87$ and $\omega\tau_0 = 10^{-4}$ with $n = 1$, where $a^{(n)}/\gamma_0$ and $b^{(n)}/\gamma_0$ are almost independent of γ_0 . This behavior is consistent with that for the number of contact changes during the last cycle as shown in Ref. [36].

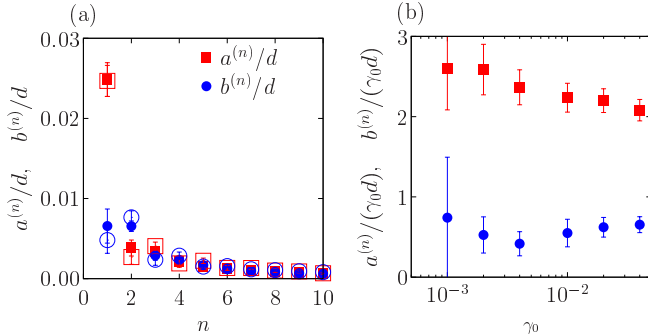


FIG. 5: (a) Magnitudes of Fourier coefficients $a^{(n)}$ and $b^{(n)}$ against n for $\phi = 0.87$ and $\gamma_0 = 0.02$ with $\omega\tau_0 = 10^{-4}$ (filled symbols) and 10^{-5} (open symbols). (b) Magnitudes of the Fourier coefficients $a^{(n)}$ and $b^{(n)}$ normalized by γ_0 against γ_0 for $\phi = 0.87$ and $\omega\tau_0 = 10^{-4}$ with $n = 1$. $\phi = 0.87$ corresponds to $\phi - \phi_J = 0.029$.

Theoretical Analysis— Now, let us reproduce the numerical results by a simple analytic calculation. Substituting Eqs. (7) and (8) into Eq. (4) with Eq. (6), we obtain the expression G'_T of the storage modulus in SAS up to $O(\gamma_0, \{|\mathbf{a}_i^{(n)}|\}, \{|\mathbf{b}_i^{(n)}|\})$ as [36]

$$G'_T = -\frac{1}{L^2} \sum_{i,j} \left\langle \frac{X_{ij}^2 Y_{ij}^2}{R_{ij}} \Psi'(R_{ij}) \right\rangle - \frac{1}{L^2} \sum_{i,j} \left\langle Y_{ij}^2 \Psi(R_{ij}) \right\rangle - \frac{1}{L^2} \sum_{i,j} \left\langle \left(\frac{a_{ij,x}^{(1)}}{\gamma_0} Y_{ij} + X_{ij} \frac{a_{ij,y}^{(1)}}{\gamma_0} \right) \Psi(R_{ij}) \right\rangle - \frac{1}{L^2} \sum_{i,j} \left\langle X_{ij} Y_{ij} \Psi'(R_{ij}) \frac{\mathbf{R}_{ij} \cdot \mathbf{a}_{ij}^{(1)}}{\gamma_0 R_{ij}} \right\rangle, \quad (13)$$

where $\Psi(r) = -U'(r)/r$, $\mathbf{R}_{ij} = \mathbf{R}_i - \mathbf{R}_j = (X_{ij}, Y_{ij})$, and $\mathbf{a}_{ij}^{(1)} = \mathbf{a}_i^{(1)} - \mathbf{a}_j^{(1)}$. In the expression of Eq. (13), only the first harmonic contribution from $\mathbf{a}_i^{(1)}$ can survive because of Eq. (4). Note that \mathbf{R}_i and $\mathbf{a}_i^{(1)}$ cannot be determined within the theory but are determined by our simulation data. In Fig. 2, we plot the theoretical prediction G'_T as open symbols, which quantitatively reproduces the numerical results for the region of quite large γ_0 . The first and second terms on the right-hand side (RHS) of Eq. (13) represent the contributions from the affine transformation depending only on \mathbf{R}_i , while the third and fourth terms including $\mathbf{a}_{ij}^{(1)}/\gamma_0$ indicate the contributions from the non-affine trajectories. As shown in Ref. [36], the contributions from the non-affine trajectories are almost

independent of γ_0 , which is consistent with the behavior of $a^{(1)}/\gamma_0$ shown in Fig. 5(b). Numerical evaluation in Ref. [36] reveals that SAS is dominated by the first term on RHS of Eq. (13) through the change of \mathbf{R}_i . The center of the non-affine trajectories \mathbf{R}_i is changed by the rearrangement of the configuration during the transient to the absorbing state, which is consistent with the memory formation of dense particles during oscillatory shear [39–41].

The theoretical expression G''_T of the loss modulus in SAS up to $O(\gamma_0, \{|\mathbf{a}_i^{(n)}|\}, \{|\mathbf{b}_i^{(n)}|\})$ is given by [36]

$$G''_T = -\frac{1}{L^2} \sum_{i,j} \left\langle \left(\frac{b_{ij,x}^{(1)}}{\gamma_0} Y_{ij} + X_{ij} \frac{b_{ij,y}^{(1)}}{\gamma_0} \right) \Psi(R_{ij}) \right\rangle - \frac{1}{L^2} \sum_{i,j} \left\langle X_{ij} Y_{ij} \Psi'(R_{ij}) R_{ij} \frac{\mathbf{R}_{ij} \cdot \mathbf{b}_{ij}^{(1)}}{\gamma_0 R_{ij}^2} \right\rangle \quad (14)$$

with $\mathbf{b}_{ij}^{(1)} = \mathbf{b}_i^{(1)} - \mathbf{b}_j^{(1)}$. Similar to the case of G'_T , only the contribution of the first harmonics $\mathbf{b}_i^{(1)}$ in the expression of Eq. (8) can survive because of Eq. (5). Note that $\mathbf{b}_i^{(1)}$ cannot be determined within the theory but is evaluated by the simulation data. The loss modulus depends only on the non-affine contribution including $\mathbf{b}_i^{(1)}$. The amplitude $b^{(1)}$ remains finite in the limit $\omega \rightarrow 0$, which leads to the residual loss modulus as in Fig. 3(b). We plot the theoretical expression G''_T using the open symbols in Fig. 3(a), which also reproduces the numerical results. Thus, our theory reveals the quantitative relationship between the loss modulus and closed trajectories, which was suggested in Ref. [26].

Conclusion— We numerically studied the mechanical response of jammed materials consisting of frictionless and overdamped particles under oscillatory shear. The shear modulus exhibits SAS and the residual loss modulus exists in the quasi-static limit in the absorbing state. Through Fourier analysis of the closed trajectories, the theoretical expressions for the storage and loss moduli quantitatively agree with the numerical results.

Reference [4] reported that the loss modulus vanishes in the absorbing jammed states in the limit $\omega \rightarrow 0$, which is inconsistent with our result. It is noteworthy that Ref. [4] did not consider any transient state associated with contact changes before the system reaches the absorbing state. Since the loss modulus is expected to be given by the generalized Green-Kubo formula [42, 43], the origin of the residual loss modulus might be plastic events in the transient dynamics.

Recent studies of large amplitude oscillatory shear (LAOS) reveal that there are contributions from higher harmonics in the mechanical response of nonlinear viscoelastic materials [44, 45]. We calculate nonlinear viscoelastic moduli G'_n and G''_n with $n \geq 2$ and confirm that such higher order moduli are negligible in our system as shown in Ref. [36].

In this Letter, we focus only on the nonlinear response of disordered frictionless particles. However, even fric-

tional grains have friction and exhibit SAS depending on the friction coefficient [46]. Therefore, an extension of our theory to these systems will be our future work.

Acknowledgments

The authors thank K. Saitoh, D. Ishima, T. Kawasaki, K. Miyazaki, and K. Takeuchi for fruitful discussions.

This work was supported by JSPS KAKENHI Grant Numbers JP16H04025 and JP19K03670 and ISHIZUE 2020 of the Kyoto University Research Development Program.

[1] M. van Hecke, *J. Phys.: Condens. Matter* **22**, 033101 (2009)

[2] R. P. Behringer and B. Chakraborty, *Rep. Prog. Phys.* **82** 012601 (2019)

[3] C. S. O’Hern, S. A. Langer, A. J. Liu, and S. R. Nagel, *Phys. Rev. Lett.* **88**, 075507 (2002).

[4] B. P. Tighe, *Phys. Rev. Lett.* **107**, 158303 (2011).

[5] M. Otsuki and H. Hayakawa, *Phys. Rev. E* **95**, 062902 (2017).

[6] C. Coulais, A. Seguin, and O. Dauchot, *Phys. Rev. Lett.* **113**, 198001 (2014).

[7] M. Otsuki and H. Hayakawa, *Phys. Rev. E* **90**, 042202 (2014).

[8] K. Hima Nagamanasa, S. Gokhale, A. K. Sood, and R. Ganapathy, *Phys. Rev. E* **89**, 062308 (2014).

[9] E. D. Knowlton, D. J. Pine, and L. Cipelletti, *Soft Matter* **10**, 6931 (2014).

[10] T. Kawasaki and L. Berthier, *Phys. Rev. E* **94**, 022615 (2016).

[11] P. Leishangthem, A. D. S. Parmar, and S. Sastry, *Nat. Commun.* **8**, 14653 (2017).

[12] A. H. Clark, J. D. Thompson, M. D. Shattuck, N. T. Ouellette, and C. S. O’Hern, *Phys. Rev. E* **97**, 062901 (2018).

[13] J. Boschan, S. Luding, and B. P. Tighe, *Granul. Matter* **21**, 58 (2019).

[14] H. Hinrichsen, *Adv. Phys.* **49**, 815 (2000).

[15] M. Henkel, H. Hinrichsen, and S. Lubeck, *Nonequilibrium Phase Transition I: Absorbing Phase Transitions* (Springer, Heidelberg, 2008).

[16] D. J. Pine, J. P. Collub, J. F. Brady, and A. M. Leshansky, *Nature* (London) **438**, 997 (2005).

[17] L. Corté, P. M. Chaikin, J. P. Gollub, and D. J. Pine, *Nature Phys.* **4**, 420 (2008).

[18] J. Boschan, D. Vägberg, E. Somfai, and B. P. Tighe, *Soft Matter* **12**, 5450 (2016).

[19] D. Nakayama, H. Yoshino, and F. Zamponi, *J. Stat. Mech.* **2016** 104001 (2016).

[20] T. Kawasaki and K. Miyazaki, arXiv:2003.10716.

[21] S. Dagois-Bohy, E. Somfai, B. P. Tighe, and M. van Hecke, *Soft Matter* **13**, 9036 (2017).

[22] D. Ishima and H. Hayakawa, *Phys. Rev. E* **101**, 042902 (2020).

[23] M. Lundberg, K. Krishan, N. Xu, C. S. O’Hern, and M. Dennin, *Phys. Rev. E* **77**, 041505 (2008).

[24] C. F. Schreck, R. S. Hoy, M. D. Shattuck, and C. S. O’Hern, *Phys. Rev. E* **88**, 052205 (2013).

[25] N. C. Keim and P. E. Arratia, *Soft Matter* **9**, 6222 (2013).

[26] N. C. Keim and P. E. Arratia, *Phys. Rev. Lett.* **112**, 028302 (2014).

[27] I. Regev, T. Lookman, and C. Reichhardt *Phys. Rev. E* **88**, 062401 (2013).

[28] I. Regev, J. Weber, C. Reichhardt, K. A. Dahmen, and T. Lookman, *Nat. Commun.* **6**, 8805 (2015).

[29] N. V. Priezjev, *Phys. Rev. E* **93**, 013001 (2016).

[30] M. O. Lavrentovich, A. J. Liu, and S. R. Nagel, *Phys. Rev. E* **96**, 020101(R) (2017).

[31] K. Nagasawa, K. Miyazaki and T. Kawasaki, *Soft Matter* **15**, 7557 (2019).

[32] P. Das, H. A. Vinutha, and S. Sastry, *Proc. Natl. Acad. Sci. USA* **117**, 10203 (2020).

[33] K. Khirallah, B. Tyukodi, D. Vandembroucq, and C. E. Maloney, *Phys. Rev. Lett.* **126**, 218005 (2021).

[34] M. S. van Deen, J. Simon, Z. Zeravcic, S. Dagois-Bohy, B. P. Tighe, and M. van Hecke, *Phys. Rev. E* **90**, 020202(R) (2014).

[35] D. J. Evans and G. P. Morriss, *Statistical Mechanics of Nonequilibrium Liquids* 2nd ed. (Cambridge University Press, Cambridge, 2008).

[36] See Supplemental Material.

[37] M. Doi and S. F. Edwards, *The Theory of Polymer Dynamics* (Oxford University Press, Oxford, 1986).

[38] M. Meyers and K. Chawla, *Mechanical Behavior of Materials* (Cambridge University Press, Cambridge, 2008).

[39] D. Fiocco, G. Foffi, and S. Sastry, *Phys. Rev. Lett.* **112**, 025702 (2014).

[40] J. D. Paulsen, N. C. Keim, and S. R. Nagel, *Phys. Rev. Lett.* **113**, 068301 (2014).

[41] M. Adhikari and S. Sastry, *Eur. Phys. J. E* **41**, 105 (2018).

[42] S-H. Chong, M. Otsuki, and H. Hayakawa, *Phys. Rev. E* **81**, 041130 (2010).

[43] H. Hayakawa and M. Otsuki, *Phys. Rev. E* **88**, 032117 (2013).

[44] M. H. Wagner, V. H. Rolón-Garrido, K. Hyun, and M. Wilhelm, *J. Rheol.* **55**, 495 (2011).

[45] K. Hyun, M. Wilhelm, C. O. Klein, K. S. Cho, J. G. Nam, K. H. Ahn, S. J. Lee, R. H. Ewoldt, and G. H. McKinley, *Prog. Polym. Sci.* **36**, 1697 (2011).

[46] M. Otsuki and H. Hayakawa, *Eur. Phys. J. E* **44**, 70 (2021).

Supplemental Material:

This Supplemental Material provides some details that are not written in the main text. The results for underdamped frictionless granular particles without background friction are presented in Sec. I. In Sec. II, we present the time evolution of the displacements of particles before reaching the absorbing state and the evaluation of the yielding strain amplitude γ_c . In Sec. III, we illustrate the time evolutions of the stress-strain curves in the absorbing and plastic states. In Sec. IV, we show how particle trajectories depend on γ_0 and ω . In Sec. V, we show that trajectories in the absorbing state with longer periods do not affect our theoretical results based on the absorbing trajectories whose periods are identical to the period of the external oscillation. In Sec. VI, we present the loss modulus in the absorbing and plastic states. In Sec. VII, we demonstrate how the naive result of the Kelvin–Voigt model can be recovered for sufficiently small strain amplitude. In Sec. VIII, we illustrate the relation between the Fourier coefficients and the shape of particle trajectories. In Sec. IX, we show the number of contact changes during the last cycle in the absorbing state. In Sec. X, we derive Eqs. (13) and (14) in the main text. In Sec. XI, we decompose the storage and loss moduli into several components, and clarify what components are dominant contributions for the storage and loss moduli. In Sec. XII, we show the nonlinear viscoelastic moduli in our system to clarify the roles of higher harmonics.

I. UNDERDAMPED GRANULAR PARTICLES

In this section, we show that our results are qualitatively unchanged in underdamped frictionless granular particles without background friction. Here, we use the SLLOD equation given by [34]

$$\frac{d}{dt}\mathbf{r}_i = \dot{\gamma}(t)y_i\mathbf{e}_x + \mathbf{p}_i, \quad (\text{S1})$$

$$\frac{d}{dt}\mathbf{p}_i = -\dot{\gamma}(t)p_{i,y}\mathbf{e}_x + \mathbf{F}_i \quad (\text{S2})$$

under the Lees–Edwards boundary condition, where $\mathbf{p}_i = m(\dot{\mathbf{r}}_i - \dot{\gamma}(t)y_i)\mathbf{e}_x$ and

$$\mathbf{F}_i = -\sum_{j \neq i} \frac{\partial}{\partial \mathbf{r}_i} U(r_{ij}) - \sum_{j \neq i} \eta v_{ij}^{(n)} \Theta(d_{ij} - r_{ij}) \frac{\mathbf{r}_{ij}}{r_{ij}} \quad (\text{S3})$$

with mass m , the interaction potential $U(r_{ij})$ given by Eq. (2), the viscous constant η , and the normal velocity

$$v_{ij}^{(n)} = \left\{ \frac{d}{dt}\mathbf{r}_i - \frac{d}{dt}\mathbf{r}_j \right\} \cdot \frac{\mathbf{r}_{ij}}{r_{ij}}. \quad (\text{S4})$$

We adopt $\eta = \sqrt{mk}$. This model corresponds to frictionless granular particles with the restitution coefficient $e = 0.043$. We adopt the leapfrog algorithm using the

time step $\Delta t = 0.05t_0$ with the characteristic time with $t_0 = \sqrt{m/k}$.

In Fig. S1, we plot non-affine trajectories in the last two cycles for a particle with $\gamma_0 = 0.02$, $\phi = 0.87$, and $\omega = 10^{-4}\tau_0^{-1}$ in the absorbing state. The trajectories are closed, but there is a region where the position of the particle depends on the number of cycles n_c . The result of Fig. S1 is a typical one from the inertia effect in the underdamped system.

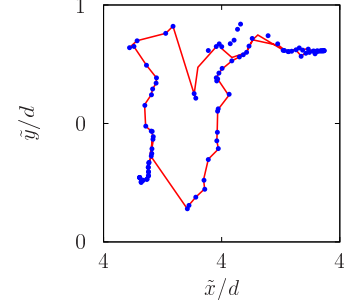


FIG. S1: Non-affine trajectories in the last two cycles for underdamped particles with $\gamma_0 = 0.02$, $\phi = 0.87$, and $\omega = 10^{-4}\tau_0^{-1}$ in the absorbing state. The circles represent the trajectory in the last cycle. The line represents the trajectory in the second to the last cycle.

Figure S2 plots the magnitude of the Fourier coefficients $a^{(n)}$ and $b^{(n)}$ against n for $\phi = 0.87$ and $\gamma_0 = 0.02$ with $\omega\tau_0 = 10^{-4}$. As in the overdamped system, $a^{(1)}$ takes the largest value, and the other components are finite. In the inset of Fig. S2, we show $a^{(1)}$ and $b^{(1)}$ against γ_0 for $\phi = 0.87$ and $\gamma_0 = 0.02$ with $\omega\tau_0 = 10^{-4}$, which are proportional to γ_0 .

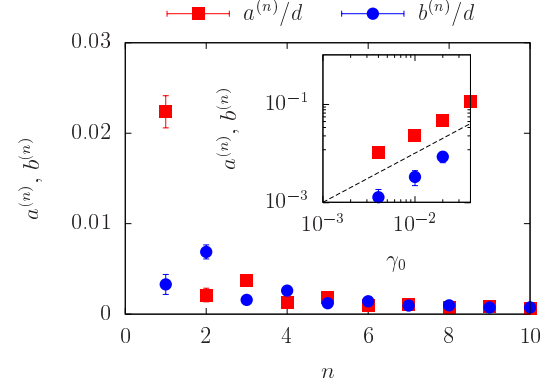


FIG. S2: Magnitudes of Fourier coefficients $a^{(n)}$ and $b^{(n)}$ of the underdamped particles against n for $\phi = 0.87$ and $\gamma_0 = 0.02$ with $\omega\tau_0 = 10^{-4}$. (Inset) Magnitudes of the Fourier coefficients $a^{(n)}$ and $b^{(n)}$ against γ_0 for $\phi = 0.87$ and $\omega\tau_0 = 10^{-4}$ with $n = 1$. The dashed line represents $a^{(1)}, b^{(1)} \propto \gamma_0$.

In Fig. S3, we plot the scaled storage modulus G' of the underdamped particles in the absorbing state against the scaled amplitude γ_0 for $\omega = 10^{-4}\tau_0^{-1}$ with $\phi = 0.870$

and 0.860. The storage modulus exhibits SAS. The corresponding theoretical expression G'_T in Eq. (13) as open symbols is also presented in Fig. S3, which quantitatively reproduces the numerical results except for the region of quite large γ_0

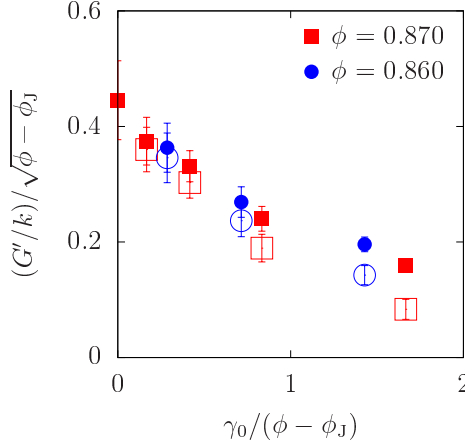


FIG. S3: Scaled storage modulus $G'/\sqrt{\phi - \phi_J}$ of underdamped particles (filled symbols) and its theoretical expression using G'_T (open symbols) in Eq. (13) against scaled $\gamma_0/(\phi - \phi_J)$ in the absorbing state scaled by the distance $\phi - \phi_J$ from the jamming point for $\omega = 10^{-4}\tau_0^{-1}$ with $\phi = 0.870$ and 0.860 .

In Fig. S4(a), we present the loss modulus G'' obtained in our simulation and its theoretical expression G''_T in Eq. (14) against γ_0 for $\omega = 10^{-4}\tau_0^{-1}$ with $\phi = 0.870$ and 0.860 in the underdamped system. The loss modulus G'' does not strongly depend on ϕ and γ_0 , and the theoretical expression G''_T reproduces the numerical results. In Fig. S4(b), we plot the loss modulus G'' against ω for $\phi = 0.87$ with $\gamma = 0.01$. The loss modulus seems to converge to a finite value in the limit $\omega \rightarrow 0$.

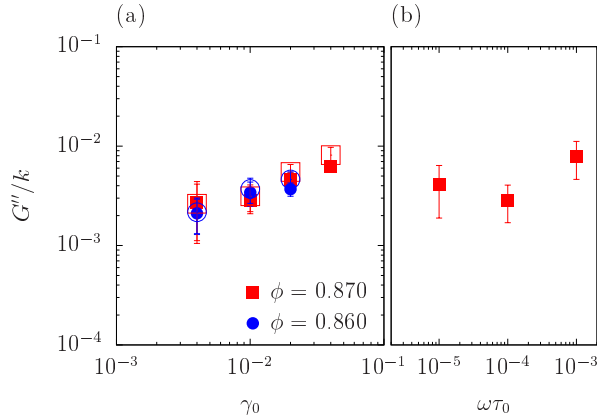


FIG. S4: (a) Loss modulus G'' of underdamped particles obtained in our simulation (filled symbols) and its theoretical expression G''_T (open symbols) in Eq. (14) against γ_0 for $\omega = 10^{-4}\tau_0^{-1}$ with $\phi = 0.870$ and 0.860 . (b) Loss modulus G'' against ω for $\phi = 0.87$ with $\gamma_0 = 0.01$.

The results in this section are consistent with those in the main text for the overdamped system. This indicates that the results presented in the main text are universal for jammed disordered materials.

II. PARTICLE DISPLACEMENT AND YIELDING STRAIN AMPLITUDE

In this section, we show the time evolution of the displacements of particles before reaching the absorbing state and the evaluation of the yielding strain amplitude γ_c . Here, we introduce the particle displacement between n_c -th and $(n_c - m)$ -th cycles as

$$dr_m(n_c) = \sum_{i=1}^N |\mathbf{r}_i(n_c T) - \mathbf{r}_i((n_c - m)T)| / N. \quad (S5)$$

with the period $T = 2\pi/\omega$. We define $dr(n_c)$ as the minimum value of $dr_m(n_c)$ for m . In Fig. S5, we plot $dr(n_c)$ against n_c for $\omega = 10^{-4}\tau_0^{-1}$ and $\phi = 0.860$ with $\gamma_0 = 0.08, 0.04$, and 0.02 . For $\gamma_0 = 0.08$, $dr(n_c)$ remains finite, while it approaches 0 after a transient for $\gamma_0 = 0.04$ and 0.02 .

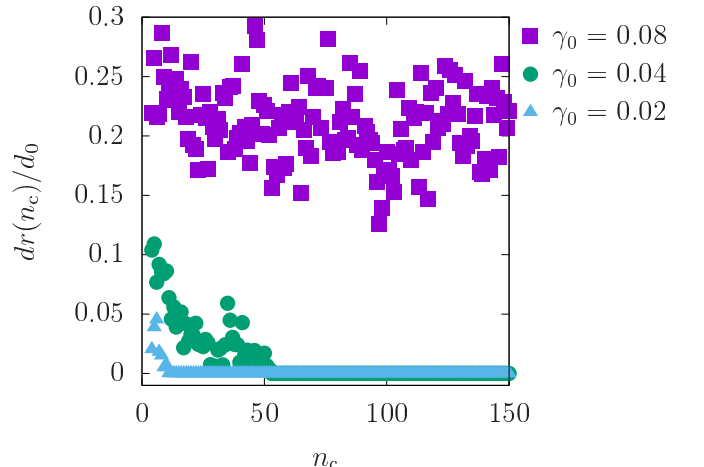


FIG. S5: Displacements of particles $dr(n_c)$ against n_c for $\omega = 10^{-4}\tau_0^{-1}$ and $\phi = 0.860$ with $\gamma_0 = 0.08, 0.04$, and 0.02 .

In Fig. S6, we plot $dr(n_c)$ against γ_0 at $n_c = 100$ for $\omega = 10^{-4}\tau_0^{-1}$ with $\phi = 0.870, 0.860, 0.850$ and 0.845 . For all ϕ , $dr(n_c)$ changes from 0 to finite values as γ_0 increases. We call the absorbing state for $dr(n_c) < d_c$ with smaller γ_0 and the plastic state for $dr(n_c) > d_c$ with larger γ_0 . The yielding strain amplitude γ_c is defined as the boundary between these states. From Fig. S6, we estimate $0.04 < \gamma_c < 0.08$ for $\phi = 0.870$, $0.04 < \gamma_c < 0.05$ for $\phi = 0.860$, $0.02 < \gamma_c < 0.03$ for $\phi = 0.850$, and $0.01 < \gamma_c < 0.02$ for $\phi = 0.845$.

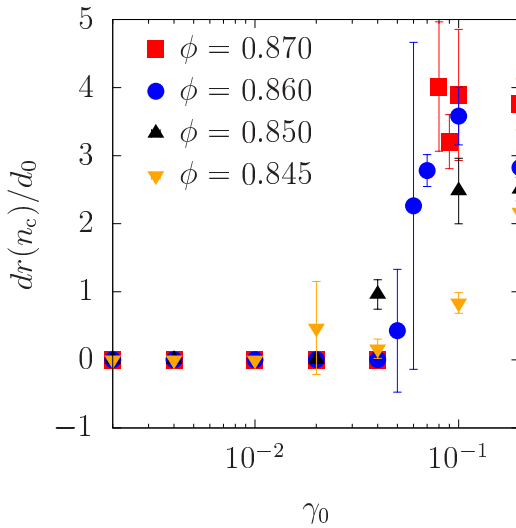


FIG. S6: Displacement of particles $dr(n_c)$ against γ_0 at $n_c = 100$ for $\omega = 10^{-4}\tau_0^{-1}$ with $\phi = 0.870, 0.860, 0.850$ and 0.845 .

III. STRESS-STRAIN CURVE

In this section, we present typical stress strain curves in the absorbing and plastic states including their time evolution. Figure S7 displays the shear stress σ against the strain γ with $\gamma_0 = 0.02$ for different n_c . For $n_c \leq 5$, the stress-strain curves are not convergent, which indicate the system is in a transient state. For $n_c = 6$ and 7 , the stress-strain curves become identical in the absorbing state. We plot the shear stress σ against the strain γ for $\gamma_0 = 0.1$ in Fig. S8. All the stress-strain curves are different for all n_c because the system is in the plastic state.

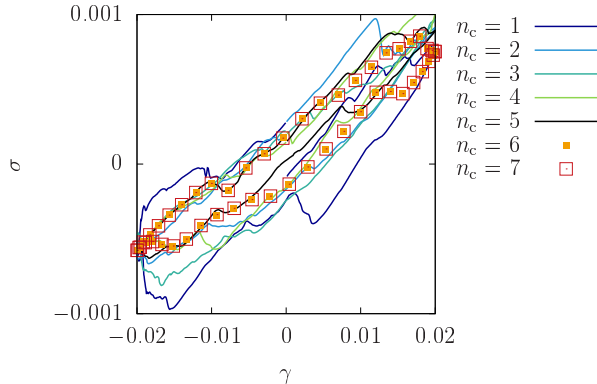


FIG. S7: Plots of shear stress σ against γ for $\gamma_0 = 0.02$, $\omega = 10^{-4}\tau_0^{-1}$, and $\phi = 0.87$ corresponding to $\phi - \phi_J = 0.029$ with various n_c .

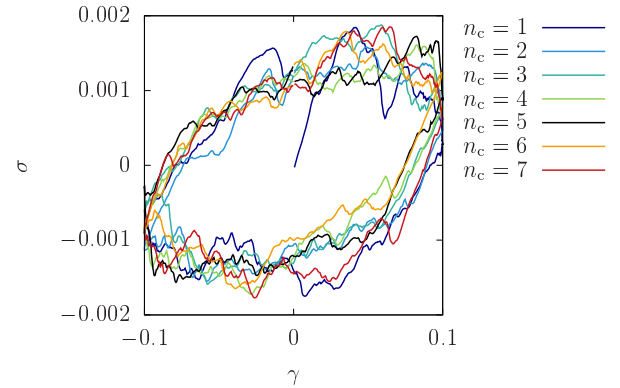


FIG. S8: Plots of shear stress σ against γ for $\gamma_0 = 0.1$, $\omega = 10^{-4}\tau_0^{-1}$ and $\phi = 0.87$ corresponding to $\phi - \phi_J = 0.029$ with various n_c .

IV. DEPENDENCE OF TRAJECTORIES ON γ_0 AND ω

In this section, we present how particle trajectories depend on γ_0 and ω . In Fig. S9, we plot the non-affine particle trajectories in the last cycle for $\omega = 10^{-3}\tau_0^{-1}$ and $10^{-5}\tau_0^{-1}$ with $\phi = 0.87$ and $\gamma_0 = 0.01$. Let us introduce

$$\mathbf{r}'_i = (x'_i, y'_i) = \tilde{\mathbf{r}}_i - \mathbf{R}_i. \quad (\text{S6})$$

The trajectories form nontrivial loops, which remain for smaller ω .

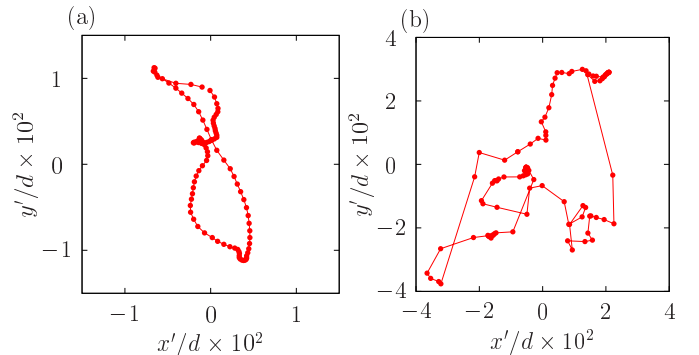


FIG. S9: Non-affine particle trajectories in the last cycle for $\omega = 10^{-3}\tau_0^{-1}$ (a) and $10^{-5}\tau_0^{-1}$ (b) with $\phi = 0.87$ and $\gamma_0 = 0.01$.

Figure S10 represents the non-affine particle trajectories in the last cycle for $\omega = 10^{-3}\tau_0^{-1}$ and $10^{-5}\tau_0^{-1}$ with $\phi = 0.87$ and $\gamma_0 = 1.0 \times 10^{-7}$. In Fig. S10 (a), the trajectory with $\omega = 10^{-3}\tau_0^{-1}$ form an ellipse, but the trajectory becomes a straight line for $\omega = 10^{-5}\tau_0^{-1}$ in Fig S10 (b).

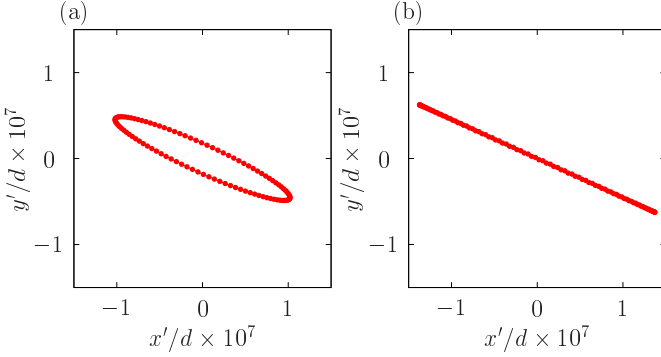


FIG. S10: Non-affine particle trajectories in the last cycle for $\omega = 10^{-3}\tau_0^{-1}$ (a) and $10^{-5}\tau_0^{-1}$ (b) with $\phi = 0.87$ and $\gamma_0 = 1.0 \times 10^{-7}$.

V. EFFECT OF TRAJECTORIES WITH LONGER PERIODS

In this section, we discuss the effect of closed trajectories with periods longer than 2π . As indicated by Refs. [27, 28, 30, 31, 33], some samples exhibit non-trivial absorbing trajectories where particles return to their original positions after more than one cycle of oscillatory shear. In these samples, the non-affine trajectories of a particle $\mathbf{r}_i(\theta)$ satisfy

$$\mathbf{r}_i(\theta) = \mathbf{r}_i(\theta + 2M\pi) \quad (S7)$$

with $M = 2, 3, 4, \dots$. In this case, $\mathbf{r}_i(\theta)$ for $0 < \theta < 2M\pi$ is expressed in the Fourier series as

$$\tilde{\mathbf{r}}_i(\theta) = \mathbf{R}'_i + \sum_{m=1}^{\infty} \left(\mathbf{A}_i^{(m)} \sin \frac{m\theta}{M} + \mathbf{B}_i^{(m)} \cos \frac{m\theta}{M} \right) \quad (S8)$$

with

$$\mathbf{R}'_i = \frac{1}{2M\pi} \int_0^{2M\pi} d\theta \tilde{\mathbf{r}}_i(\theta), \quad (S9)$$

and the Fourier coefficients

$$\mathbf{A}_i^{(m)} = \frac{1}{M\pi} \int_0^{2M\pi} d\theta \sin \frac{m\theta}{M} \tilde{\mathbf{r}}_i(\theta), \quad (S10)$$

$$\mathbf{B}_i^{(m)} = \frac{1}{M\pi} \int_0^{2M\pi} d\theta \cos \frac{m\theta}{M} \tilde{\mathbf{r}}_i(\theta). \quad (S11)$$

However, in Eqs. (4) and (5), we need $\mathbf{r}_i(\theta)$ for $0 \leq \theta < 2\pi$ to calculate G' and G'' . When $\mathbf{r}_i(\theta)$ is restricted to $0 \leq \theta < 2\pi$, we can use Eq. (8) with the Fourier coefficient given by Eqs. (10) and (11) as an expression of the trajectory, and we obtain the theoretical expressions Eqs. (13) and (14) even in this case. It should be noted that samples in the absorbing state with longer periods are rare, and the probability of emerging such a trajectory is smaller than 0.01 for sufficiently packed systems above the jamming point, as shown in Ref. [30]. Therefore, we can ignore the effect of rare samples.

VI. LOSS MODULUS

In Fig. S11, we plot the loss modulus G'' against γ_0 for $\omega = 10^{-4}\tau_0^{-1}$ with $\phi = 0.870$ and 0.860 including the data in the absorbing and plastic states. The previous studies [21, 22] reported that the loss modulus has a peak around the yield strain for an underdamped system, but the peak of G'' is not clearly visible in our overdamped system.

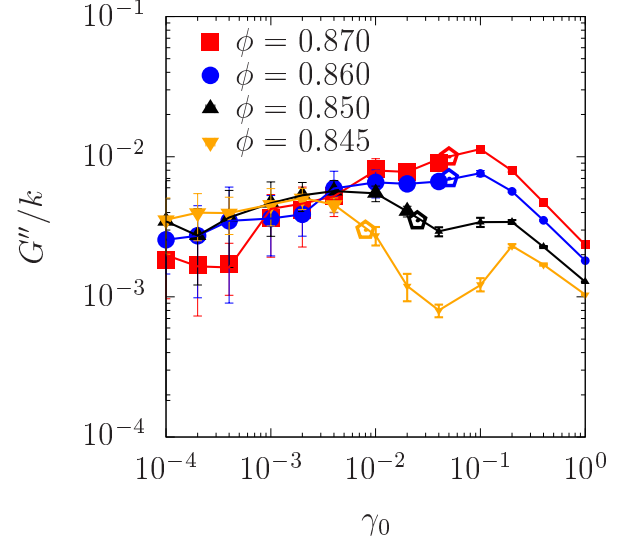


FIG. S11: Loss modulus G'' against γ_0 for $\omega = 10^{-4}\tau_0^{-1}$ with $\phi = 0.870$ and 0.860 . The larger (smaller) filled symbols represent the data in the absorbing (plastic) state. The open pentagons represent the yield strain amplitude γ_c .

VII. SHEAR MODULUS FOR SMALL γ_0

In this section, we demonstrate that G' and G'' obey the Kelvin–Voigt model for a sufficiently small γ_0 . Figure S12 is a set of plots of G' and G'' against $\omega\tau_0$ for $\phi = 0.870$ and $\gamma_0 = 1.0 \times 10^{-7}$, where G' is almost independent of ω and G'' is proportional to ω . This behavior is consistent with that of the Kelvin–Voigt model.

VIII. RELATIONSHIP BETWEEN CLOSED TRAJECTORIES AND THE FOURIER COEFFICIENTS

In this section, we present how the trajectory of a particle depends on the Fourier coefficients. Figure S13 compares the trajectory of a particle corresponding to Fig. 1(a) with its approximate trajectory using Eq. (8) with some restricted modes, where we estimate the coefficients using the true trajectory. In Fig. S13 (a), we plot the approximate trajectory (blue filled circles) using only $\mathbf{a}_i^{(1)}$, where we set the other coefficients to 0. The approximate

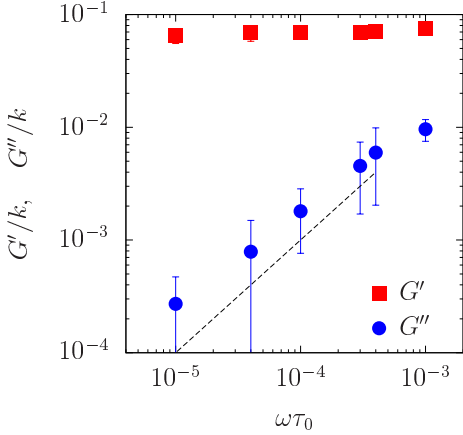


FIG. S12: Plots of G' and G'' against ω for $\phi = 0.870$ and $\gamma_0 = 1.0 \times 10^{-7}$. The dashed line represents $G'' \propto \omega$.

trajectory (blue filled circles) is a straight line. Figure S13 (b) shows the approximate trajectory using $\mathbf{a}_i^{(1)}$ and $\mathbf{b}_i^{(1)}$, where the trajectory becomes an ellipse. As we increase the number of modes, the approximate trajectory approaches the true trajectory, as shown in Figs. S13 (c) and (d).

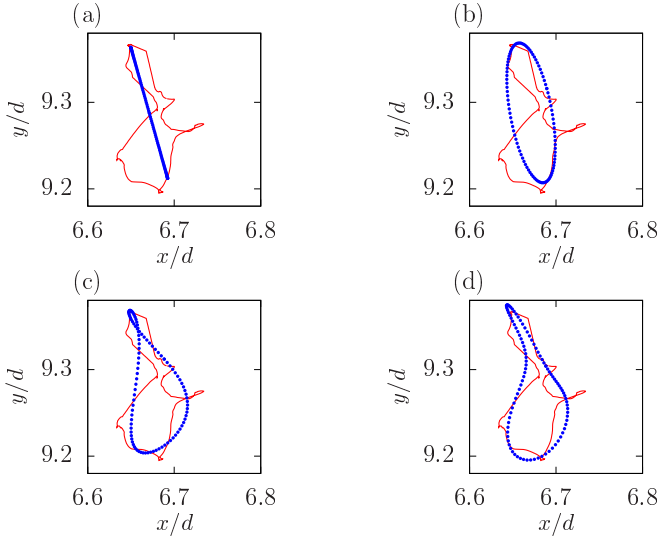


FIG. S13: Trajectory shown in Fig. 1(a) of the main text and its approximate trajectories with some restricted modes. The red solid lines represent the original data, and the blue filled circles represent the approximate trajectory using (a) $\mathbf{a}_i^{(1)}$, (b) $\mathbf{a}_i^{(1)}$ and $\mathbf{b}_i^{(1)}$, (c) $\mathbf{a}_i^{(n)}$ and $\mathbf{b}_i^{(n)}$ with $n = 1$ and 2, and (d) $\mathbf{a}_i^{(n)}$ and $\mathbf{b}_i^{(n)}$ with $n = 1, 2$, and 3.

IX. CYCLIC CONTACT CHANGES

In this section, we show the number of contact changes during the last cycle in the absorbing state. References

[21, 23, 25, 26] demonstrate that the nontrivial loops originate from cyclic open and close contacts. In Fig. S14, we present the number of cyclic contact changes N_{cc} during the last cycle for $\omega = 10^{-4}\tau_0^{-1}$ with $\phi = 0.870$ against γ_0 in the absorbing state. The number of cyclic contact changes N_{cc} is nearly proportional to γ_0 . This dependence is consistent with the behaviors of $a^{(n)}$ and $b^{(n)}$ of the Fourier components, which are almost proportional to γ_0 .

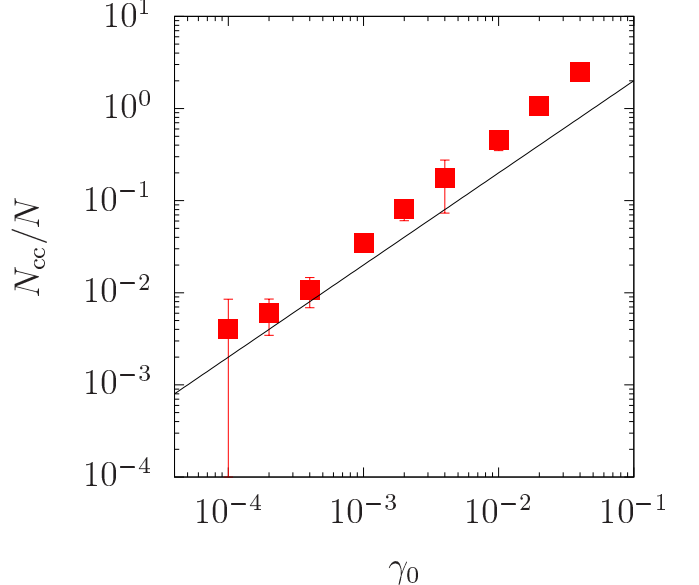


FIG. S14: The number of cyclic contact changes N_{cc} during the last cycle for $\omega = 10^{-4}\tau_0^{-1}$ with $\phi = 0.870$ against γ_0 . The solid line represents $N_{cc} \sim \gamma_0$.

X. DETAILS OF THE THEORETICAL ANALYSIS

In this section, we derive Eqs. (13) and (14) in the main text. Substituting Eq. (8) into Eq. (7), $\mathbf{r}_{ij}(\theta)$ is approximated as

$$\mathbf{r}_{ij}(\theta) \simeq \mathbf{R}_{ij} + \gamma_0 Y_{ij} \sin \theta \mathbf{e}_x + \sum_{n=1}^{\infty} \left(\mathbf{a}_i^{(n)} \sin n\theta + \mathbf{b}_i^{(n)} \cos n\theta \right) \quad (S12)$$

up to $O(\gamma_0, \{|\mathbf{a}_i^{(n)}|\}, \{|\mathbf{b}_i^{(n)}|\})$. From this equation, $r_{ij}(\theta)$ up to $O(\gamma_0, \{|\mathbf{a}_i^{(n)}|\}, \{|\mathbf{b}_i^{(n)}|\})$ is given as

$$r_{ij}(\theta) \simeq R_{ij} \{1 + E_{ij}(\theta)\}, \quad (S13)$$

where

$$E_{ij}(\theta) = \sum_{n=1}^{\infty} \frac{\mathbf{R}_{ij} \cdot \mathbf{a}_{ij}^{(n)}}{R_{ij}^2} \sin n\theta + \sum_{n=1}^{\infty} \frac{\mathbf{R}_{ij} \cdot \mathbf{b}_{ij}^{(n)}}{R_{ij}^2} \cos n\theta + \gamma_0 \frac{X_{ij} Y_{ij}}{R_{ij}^2} \sin \theta. \quad (S14)$$

Using this equation, we obtain $\Psi(r) = -U'(r)/r$ up to $O(\gamma_0, \{|\mathbf{a}_i^{(n)}|\}, \{|\mathbf{b}_i^{(n)}|\})$ as

$$\Psi(r_{ij}(\theta)) \simeq \Psi(R_{ij}) + \Psi'(R_{ij})R_{ij}E_{ij}(\theta). \quad (\text{S15})$$

Substituting Eqs. (S12)–(S15) into Eq. (6), we obtain

$$\begin{aligned} \sigma(\theta) \simeq & -\frac{1}{L^2} \sum_{(i,j)} X_{ij} Y_{ij} \Psi(R_{ij}) - \frac{1}{L^2} \sum_{(i,j)} \gamma_0 \sin \theta Y_{ij}^2 \Psi(R_{ij}) \\ & - \frac{1}{L^2} \sum_{(i,j)} \sum_{n=1}^{\infty} \left(a_{ij,x}^{(n)} \sin n\theta + b_{ij,x}^{(n)} \cos n\theta \right) Y_{ij} \Psi(R_{ij}) \\ & - \frac{1}{L^2} \sum_{(i,j)} \sum_{n=1}^{\infty} X_{ij} \left(a_{ij,y}^{(n)} \sin n\theta + b_{ij,y}^{(n)} \cos n\theta \right) \Psi(R_{ij}) \\ & - \frac{1}{L^2} \sum_{(i,j)} X_{ij} Y_{ij} \Psi'(R_{ij}) R_{ij} E_{ij}(\theta). \end{aligned} \quad (\text{S16})$$

Here, we abbreviate $\sum_i \sum_{j>i}$ as $\sum_{(i,j)}$. By substituting this equation into Eqs. (4) and (5), we obtain Eqs. (13) and (14).

XI. COMPONENTS OF SHEAR MODULI

In this section, we clarify what terms of the theoretical expressions G'_T and G''_T in the absorbing state in Eqs. (13) and (14) are dominant. Here, G'_T consists of four terms as

$$G'_T = G'_{T,1} + G'_{T,2} + G'_{T,3} + G'_{T,4} \quad (\text{S17})$$

with

$$G'_{T,1} = -\frac{1}{L^2} \sum_{i,j} \left\langle \frac{X_{ij}^2 Y_{ij}^2}{R_{ij}} \Psi'(R_{ij}) \right\rangle, \quad (\text{S18})$$

$$G'_{T,2} = -\frac{1}{L^2} \sum_{i,j} \left\langle Y_{ij}^2 \Psi(R_{ij}) \right\rangle, \quad (\text{S19})$$

$$G'_{T,3} = -\frac{1}{L^2} \sum_{i,j} \left\langle \left(\frac{a_{ij,x}^{(1)}}{\gamma_0} Y_{ij} + X_{ij} \frac{a_{ij,y}^{(1)}}{\gamma_0} \right) \Psi(R_{ij}) \right\rangle, \quad (\text{S20})$$

$$G'_{T,4} = -\left\langle \frac{1}{L^2} \sum_{i,j} X_{ij} Y_{ij} \Psi'(R_{ij}) \frac{\mathbf{R}_{ij} \cdot \mathbf{a}_{ij}^{(1)}}{\gamma_0 R_{ij}} \right\rangle, \quad (\text{S21})$$

where $G'_{T,1}$ and $G'_{T,2}$ represent the contributions from the affine motion, respectively, while $G'_{T,1}$ and $G'_{T,2}$ are the contributions from the non-affine motion, respectively. In Fig. S15, we show $G'_{T,n}$ in the absorbing state for $\omega = 10^{-4} \tau_0^{-1}$ with $\phi = 0.870$. We find that $G'_{T,1}$ and $G'_{T,4}$ are dominant. $G'_{T,1}$ decreases with γ_0 , while the other $G'_{T,n}$ with $n = 2, 3, 4$ are almost independent of γ_0 . This indicates that SAS results from the behavior of $G'_{T,1}$.

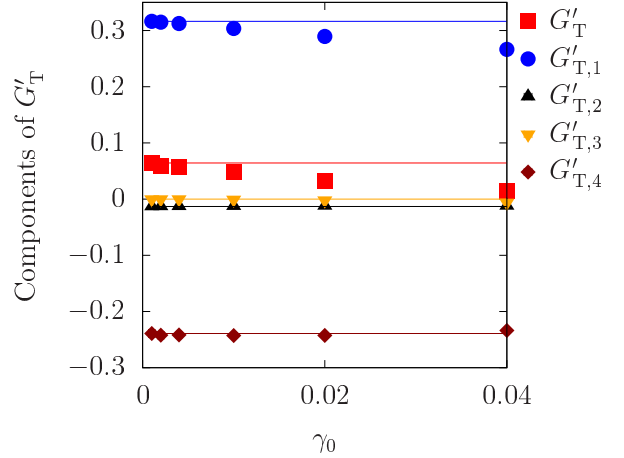


FIG. S15: $G'_{T,n}$ with $n = 1, 2, 3$ and 4 against γ_0 in the absorbing state for $\omega = 10^{-4} \tau_0^{-1}$ with $\phi = 0.870$. The horizontal lines represent $G'_{T,n}$ in the limit $\gamma_0 \rightarrow 0$, which is estimated at $\gamma_0 = 0.001$.

On the other hand, the loss modulus G''_T consists of two terms as

$$G''_T = G''_{T,1} + G''_{T,2} \quad (\text{S22})$$

with

$$G''_{T,1} = -\frac{1}{L^2} \sum_{i,j} \left\langle \left(\frac{b_{ij,x}^{(1)}}{\gamma_0} Y_{ij} + X_{ij} \frac{b_{ij,y}^{(1)}}{\gamma_0} \right) \Psi(R_{ij}) \right\rangle, \quad (\text{S23})$$

$$G''_{T,2} = -\frac{1}{L^2} \sum_{i,j} \left\langle X_{ij} Y_{ij} \Psi'(R_{ij}) R_{ij} \frac{\mathbf{R}_{ij} \cdot \mathbf{b}_{ij}^{(1)}}{\gamma_0 R_{ij}^2} \right\rangle. \quad (\text{S24})$$

In Fig. S15, we show $G''_{T,n}$ with $n = 1$ and 2 in the absorbing state for $\omega = 10^{-4} \tau_0^{-1}$ with $\phi = 0.870$. The result shows that $G''_{T,1}$ is dominant and almost independent of γ_0 . $G''_{T,2}$ depends on γ_0 , but it is much smaller than $G''_{T,1}$ for $\gamma_0 < 0.1$.

XII. NON-LINEAR VISCOELASTIC MODULI

In this section, we examine the non-linear viscoelastic moduli in our system. The nonlinear elastic response is generally characterized by nonlinear viscoelastic moduli G'_n and G''_n satisfying [41, 42]

$$\sigma(t) = \gamma_0 \sum_{n=1} \{G'_n \sin(n\omega t) + G''_n \cos(n\omega t)\}. \quad (\text{S25})$$

The storage and loss moduli are, respectively, given by $G' = G'_1$ and $G'' = G''_1$. G'_n and G''_n for $n \geq 2$ represent higher harmonics. In Figs. S17 and S18, we plot G'_n and G''_n in the absorbing state for $\omega = 10^{-4} \tau_0^{-1}$ and $\phi = 0.870$ with $n = 1, 2$, and 3, respectively. These figures indicate that the higher harmonics are negligible in our system.

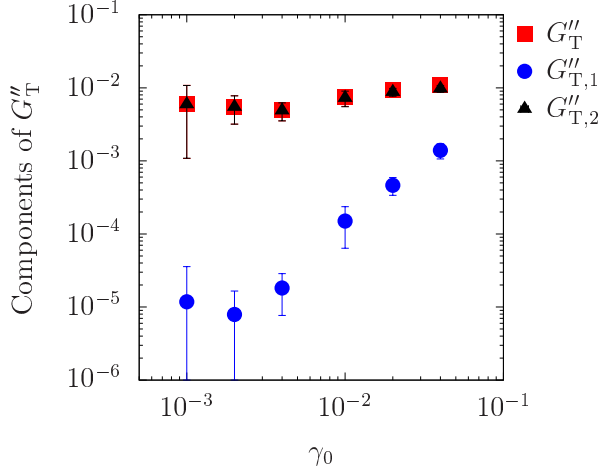


FIG. S16: $G'_{T,n}$ with $n = 1$ and 2 against γ_0 in the absorbing state for $\omega = 10^{-4}\tau_0^{-1}$ with $\phi = 0.870$.

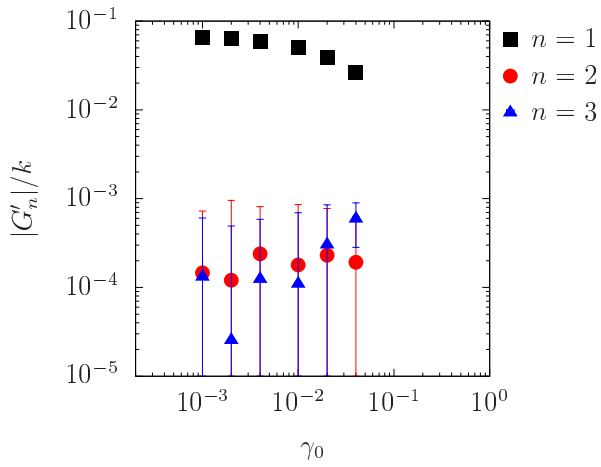


FIG. S17: G'_n against γ_0 in the absorbing state for $\omega = 10^{-4}\tau_0^{-1}$ and $\phi = 0.870$ with $n = 1, 2$, and 3 .

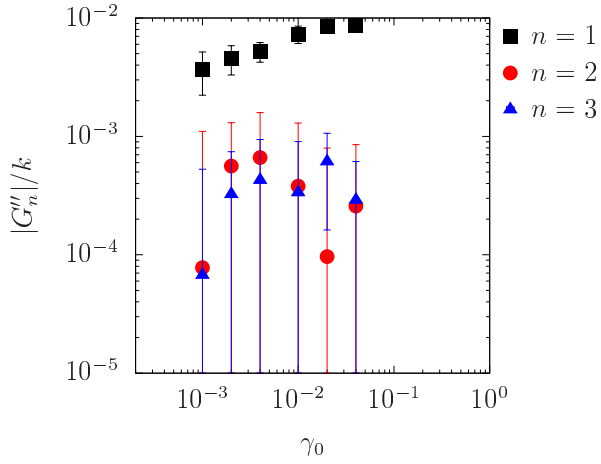


FIG. S18: G''_n against γ_0 in the absorbing state for $\omega = 10^{-4}\tau_0^{-1}$ and $\phi = 0.870$ with $n = 1, 2$, and 3 .